Proceedings of the Thirty-sixth (2026) International Ocean and Polar Engineering Conference **www.isope.org**
Orlando, Florida, USA, May 31-June 5, 2026

ISBN 978-1-880653-72-2; ISSN 1098-6189

Wall Shear Stress from a Jetting Bubble Near a Protruding-Cone Boundary

Wentao Wu[1], Chen Niu[2], Jianhua Wang[1] and Decheng Wan[1]*

[1] Computational Marine Hydrodynamics Lab (CMHL), School of Ocean and Civil Engineering,
Shanghai Jiao Tong University, Shanghai, China
[2] Wuhan Second Ship Design and Research Institute, Wuhan, China
[*]Corresponding author

ABSTRACT

The dynamics of bubbles near protruded boundaries and the resulting wall shear stress play a critical role in cavitation mechanisms relevant to ultrasonic cleaning. In this study, the well-validated Volume of Fluid (VOF) method in OpenFOAM was employed within an improved two-dimensional axisymmetric computational domain to investigate wall shear stress induced by a bubble near a conical boundary under the reference condition ($\beta = 90^{o}$, $\gamma = 1.0$). The results show that the bubble near the conical boundary generates a substantially faster micro-jet, with a velocity of $U_{jet}\approx 260$ m/s. In contrast, for a flat rigid wall ($\beta = 180^{o}$), the bubble jet velocity is only about $U_{jet}\approx 80$ m/s. Analysis of the spatio-temporal distribution of wall shear stress indicates that the peak stress near the conical boundary reaches 1034 kPa, whereas for the flat wall it is only 140 kPa, roughly seven times lower. These results highlight the significant influence of boundary geometry on bubble jet dynamics and the associated wall mechanical response.

KEY WORDS: wall shear stress; bubble dynamics; cavitation.

INTRODUCTION

Bubble dynamics plays an important role in naval architecture and ocean engineering. Cavitation is often considered detrimental, as it can cause erosion in hydraulic machinery, propellers, and hydrofoils, and generate strong loads during underwater explosions (Zhang, 2024). At the same time, controlled bubble oscillations enable useful applications, including low-frequency air guns for deep-sea exploration (Wang, 2024)and bubble-assisted ice-breaking for polar navigation (Cui， 2018). In this work, we examine the shear forces produced by bubble-induced shear flows acting on nearby surfaces, providing insights into the mechanisms of energy transfer in these scenarios. The results are also relevant to applications such as surface cleaning and cell membrane poration, where bubble-driven shear plays a key role.

The shear flow induced by bubbles on flat walls was first investigated experimentally (Ohl, 2006; Gonzalez-Avila, 2011) and later quantified in subsequent studies (Dijkink, 2008), which reported short-lived peak shear stresses of up to approximately 3.5 kPa immediately following jet impact. Numerical simulations by Zeng (2018) further indicated that, under certain conditions, these shear stresses could reach values as high as 100 kPa. In the present study, we extend the focus from flat walls to non-flat, protruding surfaces, specifically examining wall shear stresses induced by bubble jets. In our previous work (Wu, 2025), the protruding surface was simplified as a conical boundary with an apex angle β, and numerical analyses were conducted within a two-dimensional axisymmetric domain. Building on this framework, the phenomenon of enhanced jet velocity outside the conical surface, relative to a rigid flat wall, has been systematically evaluated. For instance, under a dimensionless stand-off distance of γ=1.0, the jet velocity U_{jet} reaches approximately 360 m/s for $\beta = 90^{o}$, whereas it is only 97 m/s for β=180 ^{o} . Zeng (2022) pointed out that an increase in the jet velocity U_{jet} can significantly enhance shear effects. Therefore, given the pronounced influence of U_{jet} on wall shear stress outside the cone boundary, this velocity enhancement may further amplify the shear on protruding surfaces, thereby exerting a substantial modulating effect on the local fluid dynamic characteristics.

In this study, numerical simulations were conducted using a solver whose validity has been thoroughly verified. The primary case was set with a dimensionless stand-off distance γ=1.0 and a cone angle $\beta = 90^{o}$, while a rigid-wall configuration (β = 180^{o} , γ=1.0) was employed for comparison. Building upon this setup, the computational mesh was further refined, particularly in the region near the cone tip. Subsequently, the flow field near the boundary was analyzed in detail to elucidate the key flow features responsible for generating wall shear stress. Finally, a spatio-temporal map of the wall shear stress distribution is presented, and its temporal and spatial characteristics are examined in depth.

METHODOLOGY

Numerical method

In this study, we perform numerical simulations to reconstruct the dynamics of laser-induced cavitation bubbles and to quantify the transient wall shear stresses arising during bubble oscillation. The flow is treated using a single-phase compressible formulation in which both liquid and gas share a unified velocity field, while the liquid--gas interface is captured with the Volume-of-Fluid (VOF) method. This approach allows the simultaneous representation of strongly inertial liquid motion and the compressibility of the gas within the bubble.

The flow is governed by the compressible mass and momentum conservation equations,

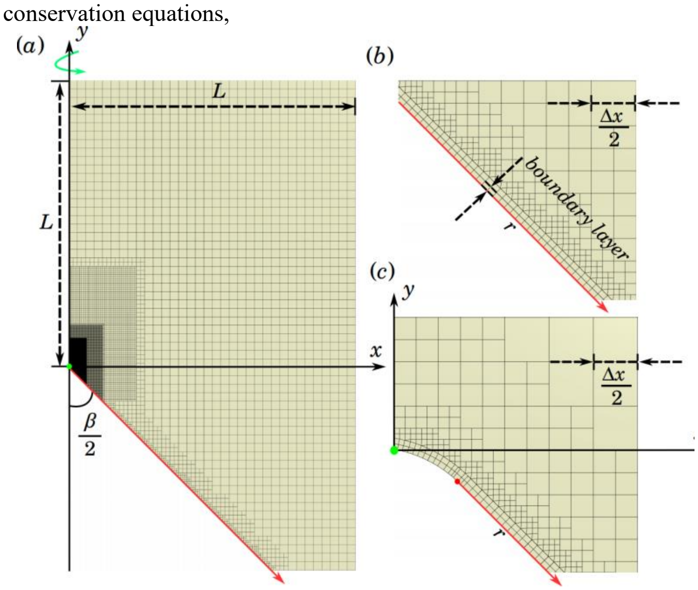

Fig.1 (a) The computational domain is two-dimensional and axisymmetric, with the *xy* plane defining the coordinate system. The origin is indicated by a green dot. The radial distance along the wall surface is represented by the red arrow *r*, with its positive direction aligned with the arrow. (b) The refined mesh region for capturing wall shear stress, where the largest cells correspond to the first level of refinement with a size of $\Delta x/2$. Here, $\Delta x/2$ denotes the mesh resolution in the primary oscillation region of the bubble. (c) The improved mesh distribution around the conical tip.

$$\frac{\partial \rho}{\partial t}+\nabla\cdot(\rho \mathbf{U}) = 0, \tag{1}$$

$$\frac{\partial (\rho \mathbf{U})}{\partial t}+\nabla\cdot(\rho \mathbf{U}\otimes\mathbf{U}) = -\nabla p+\rho\mathbf{g}+\nabla\cdot\mathbf{T}+\mathbf{f}_\sigma= 0. \tag{2}$$

Here, $\rho(\mathbf{x},t)$, $\mathbf{U}(\mathbf{x},t)$, $p(\mathbf{x},t)$ denote the density, velocity, and pressure, with $\mathbf{x}$ and t representing space and time. The gravitational acceleration is $\mathbf{g}$ and the viscous stress tensor for a Newtonian fluid is $\mathbf{T}=\mu[\nabla\mathbf{U}+(\nabla\mathbf{U})^T-(2/3)(\nabla\cdot\mathbf{U})\mathbf{I}]$, where μ is the dynamic viscosity and $\mathbf{I}$ is the identity tensor. The surface-tension force $\mathbf{f}_\sigma$is incorporated via the Continuous-Surface-Force (CSF) model, expressed as $\mathbf{f}_\sigma(\mathbf{x},t)=\int_{S(t)}\sigma\,\kappa(\mathbf{x}')\mathbf{n}(\mathbf{x}')\delta(\mathbf{x}-\mathbf{x}')\,dS'$, where σ=0.0725 N/m is the surface-tension coefficient, κ is twice the mean curvature, $\mathbf{n}$ is the unit normal pointing from gas to liquid, and δ is the Dirac delta function. In practice, the volumetric representation reduces to $\mathbf{f}_\sigma=\sigma\kappa_V\nabla\alpha_l$,with κ_V reconstructed from the liquid volume fraction α_l.

The dynamics are primarily governed by liquid inertia and gas compressibility, while viscous effects are confined to thin regions near the interface. The cavitation bubble is initialized as a small high-pressure pocket of non-condensable gas. The interface is captured through the transport equation for α_l,

$$\frac{\partial \alpha_l}{\partial t}+\nabla\cdot(\alpha_l\mathbf{U})+\nabla\cdot(\mathbf{U}_r\alpha_l\alpha_g)=\alpha_l\alpha_g\left(\frac{\psi_g}{\rho_g}-\frac{\psi_l}{\rho_l}\right)\frac{Dp}{Dt}+\alpha_l\nabla\cdot\mathbf{U}, \tag{3}$$

where $\alpha_g = 1-\alpha_l$ is the gas volume fraction, $\mathbf{U}_r$ is the interface-compression velocity, and ψ_l and ψ_g are the compressibility coefficients of liquid and gas. The material derivative of pressure is denoted by Dp/Dt. Within each mesh cell, the constraint $\alpha_l+\alpha_g=1$

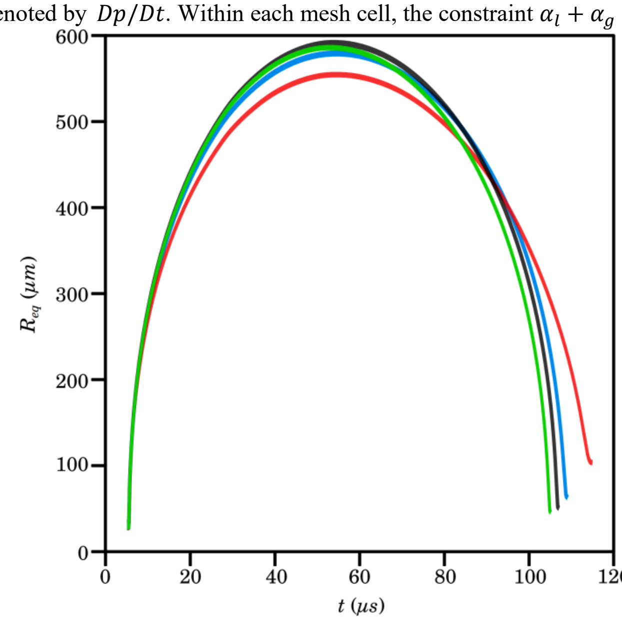

Fig.2 Comparison of the numerical results for γ=1.0 , $\beta = 90^{\circ}$ (blue curve), γ=1.0, $\beta = 180^{\circ}$ (red curve), and a bubble in free field (green curve), together with the theoretical solution obtained from the Gilmore model (black curve).

is strictly enforced. The local viscosity is computed as $\mu=\alpha_l\mu_l+\alpha_g\mu_g$, where μ_l and μ_g are the dynamic viscosities of the liquid and gas, and the density is similarly given $\rho=\alpha_l\rho_l+\alpha_g\rho_g$, with ρ_l and $\rho_g$denoting the densities of the respective phases. The density and pressure of each phase are related via the Tait equation of state:

$$\rho(p)=\rho_{i,n}\left(\frac{p+B_i}{p_{i,n}+B_i}\right)^{\frac{1}{n_{i,T}}},\quad i=g,l \tag{4}$$

where $p_{i,n}$ and $\rho_{i,n}$ are reference values at normal conditions, $n_{i,T}$ is the ratio of specific heats, and B_i is the Tait pressure parameter for each phase.

Numerical setup

The governing equations have been implemented in the open-source CFD software OpenFOAM and validated against experimental data (Wu, 2025). The present simulations follow our previous setup, with an optimized computational mesh. The two-dimensional axisymmetric domain and relevant parameters are shown in Fig.1, where the domain exhibits a regular polygonal structure in the *xy* plane. To ensure accurate resolution of the gas--liquid interface near the cone apex, a smooth, highly continuous conical tip replaces the previously sharp apex. The tip surface is tangential to the wall, with the tangency point marked by a red dot in Fig.1(c); the origin (0,0,0) is indicated by a green dot. Half of the cone angle $\beta = 90^{\circ}$ is annotated, and β can be adjusted to represent a rigid flat wall $\beta = 180^{\circ}$ for comparison. The red arrow *r* indicates the radial direction of the conical wall. Approximate non-reflecting boundary conditions are applied at a distance $L\geq 30R_{max}$ from the boundaries. The mesh near the bubble has a resolution of $\Delta x\approx$2.00 μm, and the wall-shear boundary layer thickness is 0.125 μm (Fig.1(b)(c)). The initial bubble center is located at (0, *d*, 0), at a distance *d* from the cone apex. The maximum bubble radius R_{max} is estimated from its free-field expansion, yielding the dimensionless stand-off distance γ=d/R_{max}. The bubble is initialized as a high-pressure, stationary sphere with R_{init} = 32 μm and internal pressure $P_0 = 5\times10^8\ Pa$,

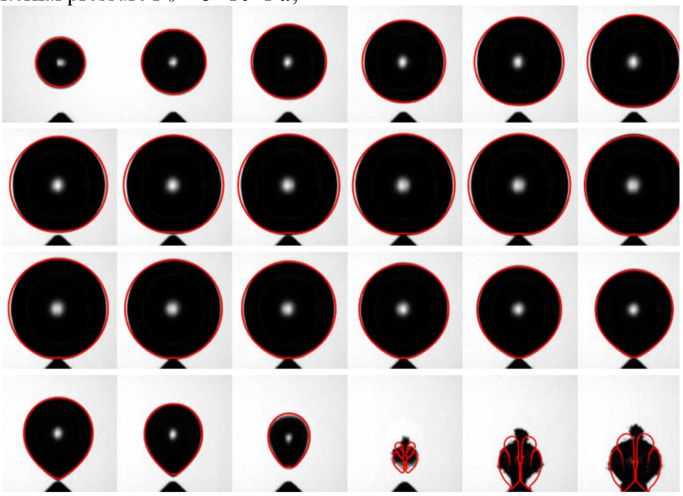

Fig.3 Comparison of the numerical results obtained on the refined mesh with experimental observations (Wu, 2025). In each image, the red contour represents the gas–liquid interface predicted by the simulation, while the background shows the corresponding experimental data. The images have a height of 1330 μm, serving as a reference scale. The time steps illustrate the bubble oscillation: the first frame corresponds to 5 μs, and subsequent frames are spaced at 5 μs intervals.

in a quiescent liquid at far-field pressure $P_\infty = P_{l,n}$ = 101325Pa.

RESULES AND DISCUSSION

We first validate the numerical simulations. Fig.2 presents three representative cases: (i) γ=1.0, β = 90º (blue curve), (ii) γ=1.0, β = 180º (red curve), and (iii) a bubble in free field (green curve). For each case, the temporal evolution of the bubble equivalent radius during the first oscillation cycle is compared to assess the model's ability to capture the primary bubble dynamics. The theoretical free-field bubble response (black curve) is obtained from the Gilmore model under identical initial conditions. It should be noted that for both the free-field simulation and the theoretical solution, the bubble undergoes approximately spherical oscillations, so the equivalent radius R_{eq} coincides with the spherical bubble radius R. Then, the bubble radius evolution in the Gilmore model satisfies

$$\left(1-\frac{\dot{R}}{C}\right)R\ddot{R}+\frac{3}{2}\left(1-\frac{\dot{R}}{3C}\right)\dot{R}^2=\left(1+\frac{\dot{R}}{C}\right)H+\left(1-\frac{\dot{R}}{C}\right)\frac{R}{C}\dot{H}, \qquad (5)$$

where the overdot denotes differentiation with respect to time, i.e. $\dot{R}=0$ is the bubble wall velocity and $\ddot{R}=0$ its acceleration. The liquid sound speed is taken as C≈1500m/s. The enthalpy difference at the bubble wall H is defined by

$$H=\int_{p_\infty}^{p}\frac{dp(\rho)}{\rho}\bigg|_{r=R}, \qquad (6)$$

where the pressure--density relation follows the Tait equation of state, consistent with the numerical setup (seeing in Eq.4). The resulting ordinary differential equations (ODE) are integrated using a Runge-Kutta scheme to obtain the theoretical free-field bubble radius evolution. The initial conditions are specified as $\dot{R}=0$and R=R_{init}, with R_{init} =32 μm and the internal pressure $P_0 = 4.35\times10^8\ Pa$.

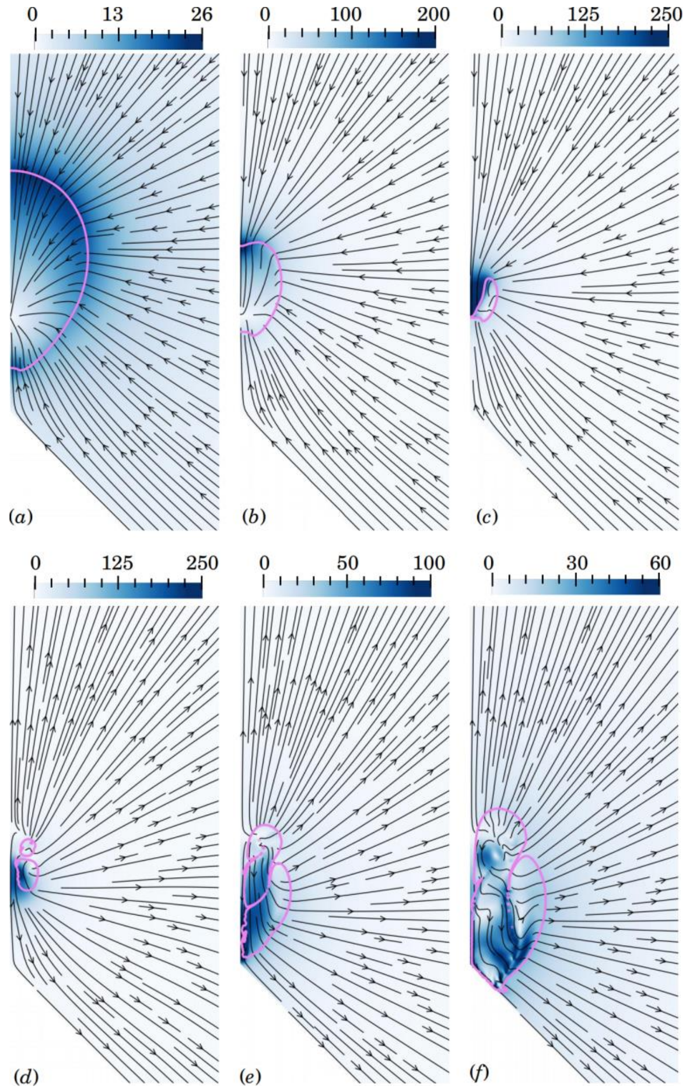

Fig.4 The velocity field during the entire process from bubble collapse to jet formation and eventual impact on the boundary is shown in Fig.1. Panels (a)–(f) correspond to the time steps t = 105, 108, 109.2, 109.6, 113, and 117μs, respectively. In each panel, the violet contours indicate the bubble interface, while the streamlines and arrows illustrate the flow direction. The colormap represents the velocity magnitude in units of m/s.

Based on the newly constructed and more structurally refined mesh, we compare the numerical simulation results with the experimental data (experimental results from Wu, 2025). As shown in Fig.3, the red contours represent the simulation results, while the background image corresponds to the experimental observations. Throughout the entire bubble oscillation process, the two exhibit excellent agreement, demonstrating the reliability of the numerical approach. For the numerical simulation corresponding to γ=1.0, β = 90º, the maximum bubble radius R_{max}≈582 μm, while the experimental measurement yields R_{max}≈575 μm.

The detailed dynamics of bubble collapse and jet formation have been thoroughly discussed in our previous work. In this study, we focus on the bubble-induced wall shear stress under the conditions of stand-off distance parameter γ=1.0 and cone angle β = 90^{o} . For comparison, the

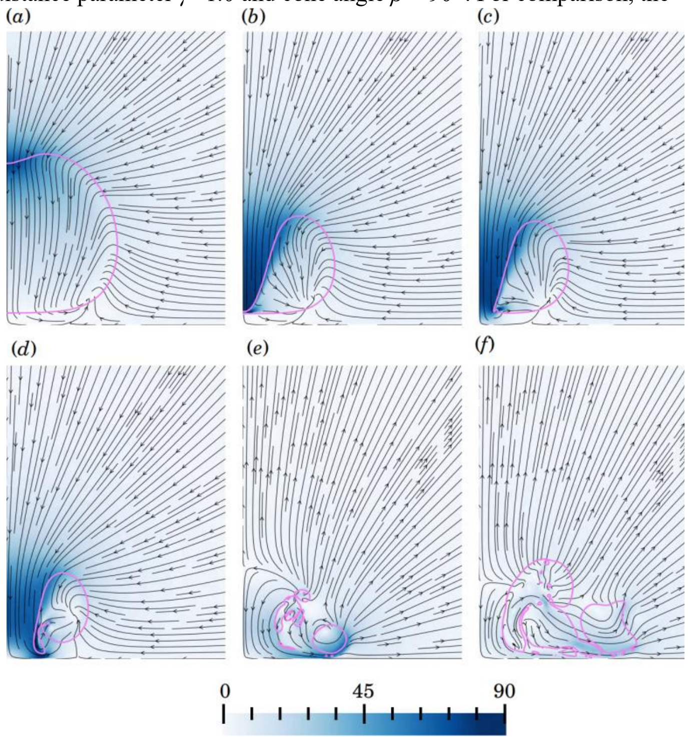

Fig.5 The velocity field throughout the entire sequence—from bubble collapse, to jet formation, and finally to jet impact on the boundary—is shown for the case of β = 180^{o} (a flat rigid wall) and γ=1.0. Panels (a)–(f) correspond to the time instants t = 104, 110.4, 111, 113, 120, and 130 μs, respectively. In each panel, the violet contours delineate the bubble interface, while the streamlines and arrows depict the flow direction. The colormap indicates the velocity magnitude in units of m/s.

case of γ=1.0 and β = 90^{o} (a flat rigid wall) is also examined. The wall shear stress is approximated as

$$\tau=\mu \frac{\partial u_r}{\partial y}\bigg|_{y=0} \approx \mu \frac{u_r(y)}{y}\Big|_{y=\delta}, \tag{7}$$

where u_r is the radial velocity component along the wall, y is the distance to the boundary, and δ is the thickness of the region with approximately constant shear rate located within the boundary layer. For the conical boundary, the definition of r is illustrated in Fig.1. The radial direction is defined as outward along the cone surface, represented by the unit vector ($sin(\beta/2)$, -$cos(\beta/2)$). Accordingly, u_r is obtained by projecting the local velocity vector onto this direction. For the flat rigid wall corresponding to β = 180^{o} , the radial direction reduces to the unit vector (1, 0). A positive wall shear stress corresponds to flow near the wall aligned with the boundary unit vector, whereas a negative value indicates flow oriented opposite to this direction.

In general, the maximum wall shear stress occurs when a bubble jet impacts the boundary. For the case with γ=1.0 and a cone angle of β = 90^{o} , the jet was identified in our previous study as a boundary-divergent regular jet. At the moment of jet ejection, a clear separation exists between the lower portion of the bubble and the boundary. During the subsequent evolution from ejection to wall impact, the jet velocity gradually decreases. To examine this process in detail, we focus on the flow near the bubble in the vicinity of the boundary. Fig.1

presents the velocity field throughout the bubble collapse. Panels (a)–(d) illustrate the sequence from bubble collapse to jet formation. The jet velocity obtained from our simulations is $U_{jet}\approx$ 260 m/s, following Wu (Wu, 2025) and Supponen et al. (Supponen, 2016), the jet velocity U_{jet} is defined as the speed at which the liquid microjet penetrates the opposite side of the bubble wall (see Fig.~4(d)). Panels (e)–(h) show the subsequent stage after the jet has pierced the lower bubble wall. During the secondary expansion of the bubble, the jet eventually impacts the boundary, at which point its velocity decreases to approximately 160 m/s.

Our previous study showed that, under a conical boundary, the bubble reaches a smaller volume at the moment of jet formation. This enhances flow convergence, generating a stronger driving pressure and thus promoting the development of a faster jet. The difference in the collapse dynamics can be clearly seen by comparing Fig.4(c) with Fig.5(b). This mechanism accounts for the higher jet velocities observed under less constrained conical geometries. By contrast, in the flat-wall configuration β = 180^{o} , the jet velocity is only $U_{jet}\approx$ 80 m/s. The corresponding jet formation and collapse process is illustrated in Fig.5. Such a pronounced difference in jet speed is expected to be directly manifested in the resulting wall shear stress.

For the six time steps shown in Fig.4, Fig.6 presents the corresponding spatial distributions of wall shear stress, analyzed in conjunction with the evolution of bubble collapse and jet formation. In panels (a)–(b), the surrounding local flow primarily drives bubble shrink, resulting in predominantly negative wall shear stresses of relatively small magnitude, indicating that the flow beneath the bubble is directed toward the boundary and exerts only moderate shear. In panel (c), although the surrounding flow still mainly drives bubble shrink (with velocities oriented negatively along the wall), the flow near the boundary is directed outward, giving rise to localized positive wall shear stress. By panel (d), the bubble jet has pierced the opposite wall, and the bubble undergoes secondary expansion, forming two anticlockwise-rotating toroidal structures, with a smaller ring enclosed by a larger one. At this stage, the flow is primarily driven by bubble expansion, directed radially outward, producing positive wall shear stress with a marked increase in magnitude. The combined action of the jet and expanding flow leads to a high-speed impact on the boundary, causing a pronounced rise in wall shear stress. As shown in Fig.6 (d), the wall shear stress near the tip of the conical boundary reaches approximately 300 kPa at the instant of jet impact. In panels (e)–(f), the two toroidal bubbles further merge, and the jet fully develops along the boundary, maintaining outward radial flow. The wall shear stress increases further, reaching values on the order of 500 kPa. During this stage, the near-wall flow is characterized by the superposition of the high-speed radial jet and the expanding bubble flow, forming complex toroidal and radial structures.

Similarly, Fig.7 shows the wall-shear-stress distributions for the reference case with β = 180^{o} and γ=1.0 at the time steps given in Fig.5. Because the liquid film between the bubble and the wall is extremely thin, the jet impacts the boundary almost immediately after emission and then propagates radially outward (see Fig.7). Owing to the relatively low jet velocity in this configuration, the peak shear stress reaches only about 100 kPa and decays rapidly with radial distance. At later stages, the bubble undergoes a secondary expansion, forming a toroidal structure adjacent to the wall and generating a counterclockwise vortex ring. This flow pattern results in predominantly positive wall shear stress, as illustrated in Fig.7(e),(f).

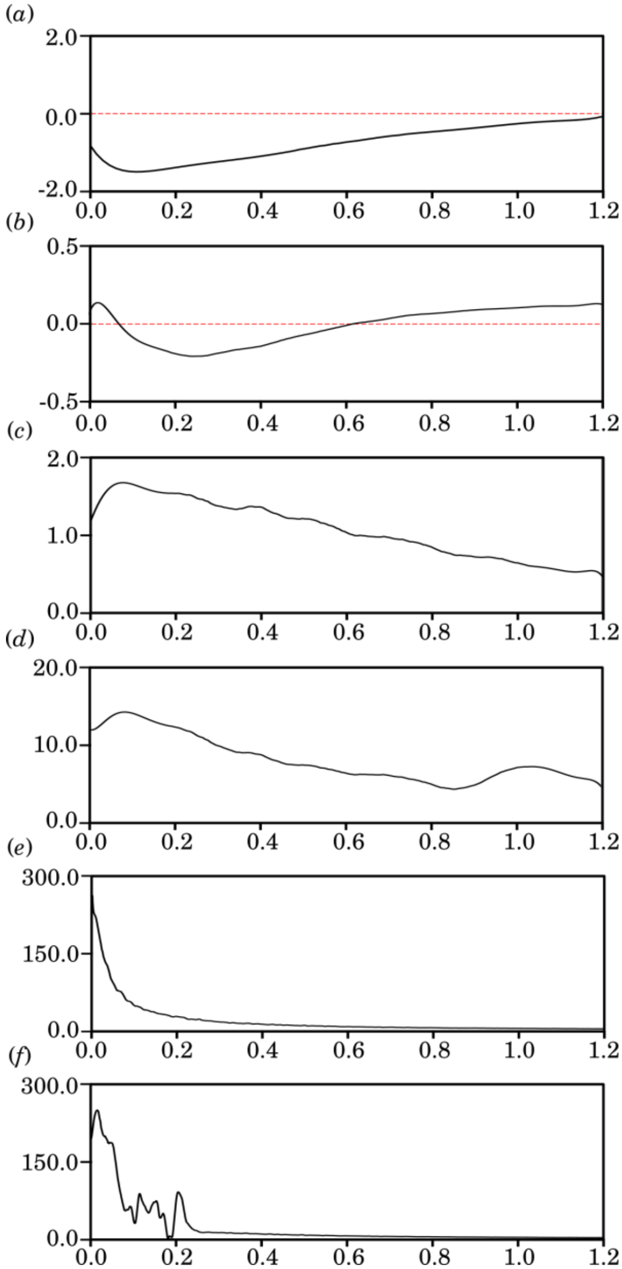

Fig.6 Distributions of wall shear stress computed from Eq.7. Each panel (a)–(f) corresponds to the time steps shown in Fig.4. The horizontal axis represents the dimensionless radial distance, r/R_{max}, while the vertical axis denotes the wall shear stress in units of kPa.

The wall shear stress analysis presented in Fig.6 can be extended to cover the entire bubble oscillation cycle. At each time step, the wall shear stress is computed and visualized as a spatiotemporal distribution,

with nondimensional time t/T_c along the horizontal axis, nondimensional radial position r/R_{max} along the vertical axis, and color indicating the magnitude of the shear stress. Due to the large range of shear stress values, a logarithmic scale is adopted for visualization, as shown in Fig.8. Panel (a) corresponds to the previously analyzed case with γ=1.0 and a cone angle of $\beta = 90^{\circ}$, whereas panel (b) presents a comparison case with γ=1.0 and β = 180 (flat rigid wall). The detailed bubble dynamics for the comparison case are not presented here but can be found in Zeng (2018).

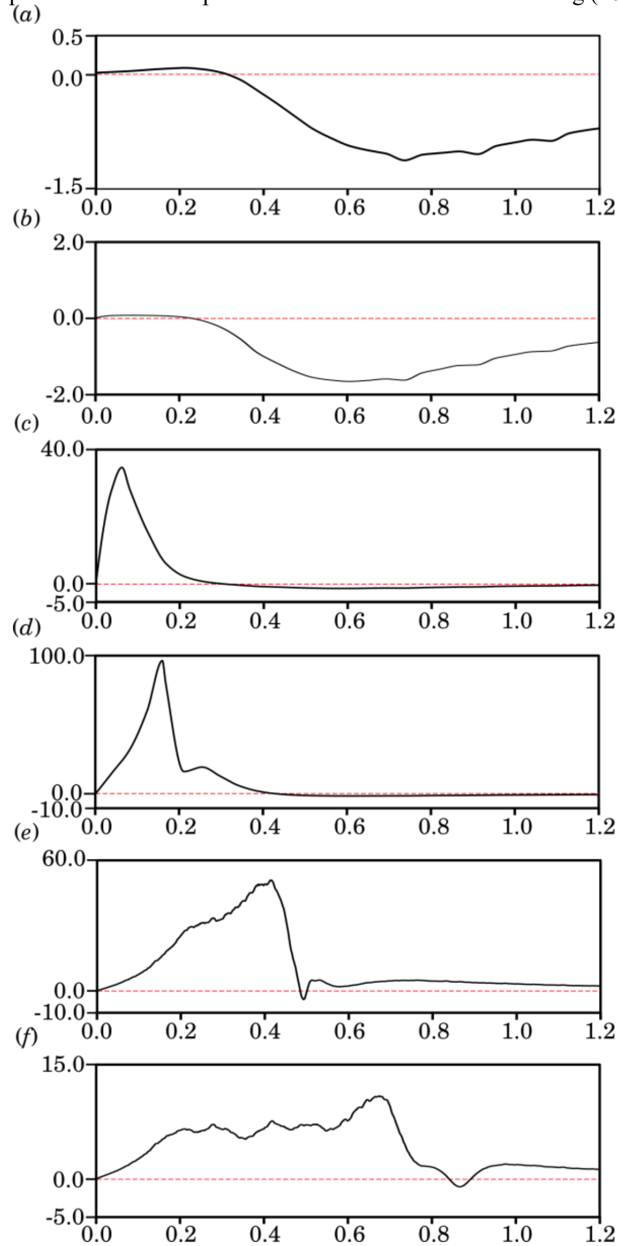

Fig.7 Distributions of the wall shear stress, panels (a)–(f) correspond to the time instants shown in Fig.5. The horizontal axis indicates the dimensionless radial distancer/R_{max}, and the vertical axis shows the wall shear stress, expressed in kPa.

For the case shown in Fig.8(a), during the early stage of bubble re-expansion (t/T_c = 0 to $t/T_c \approx 0.3$), the wall shear stress across the entire observation region remains positive, indicating that the rapidly expanding bubble drives the nearby fluid radially outward along the wall, thereby imposing a positive shear on the boundary. At a later

stage ($t/T_c \approx 0.3$), negative shear stress emerges in regions farther from the symmetry axis as the expansion slows and the fluid at larger distances begins to flow inward under the influence of the far-field pressure P_∞. In contrast, the shear stress near the axis remains positive, demonstrating that the local flow is still dominated by the expanding bubble. As the collapse progresses, the region of positive shear stress gradually contracts until jet formation. Additionally, we present the wall shear stress during the very early expansion stage, where pronounced stress peaks arise from shock waves emitted during the initial bubble growth. For the case with β = 90°, these shock-induced shear stresses are particularly strong. This shock-driven wall shear effect is consistent with experimental observations (Tomita, 1986).

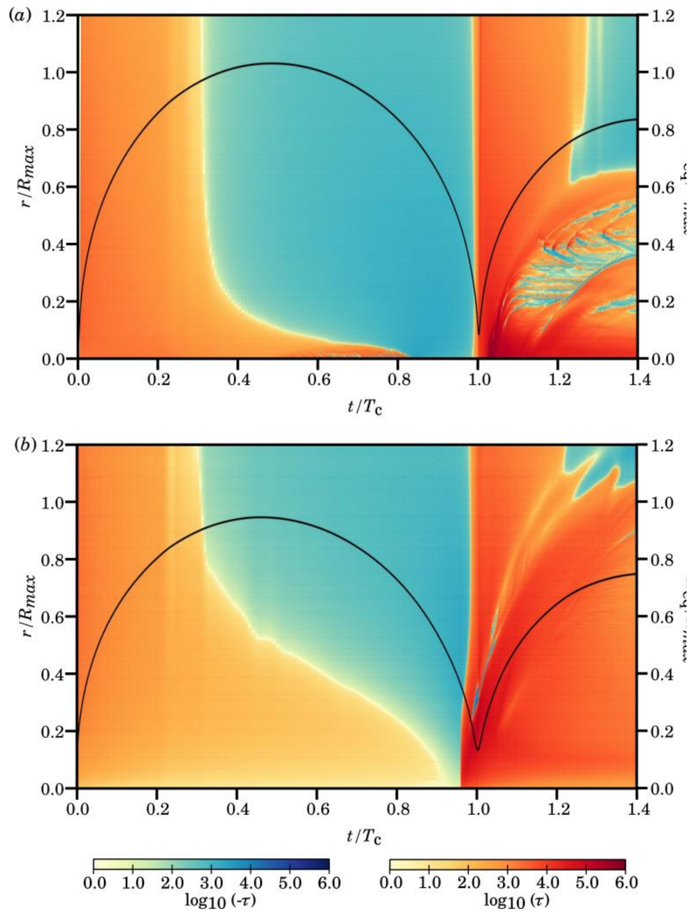

Fig.8 Time–space map of the wall shear stress for a stand-off distance $\gamma = 1.0$ and a cone angle of β = 90°. The right colour bar indicates positive wall shear stress (directed away from the axis of symmetry), while the left colour bar corresponds to negative shear stress. The unit of τ is Pa. The black solid curve denotes the RT curve of the bubble dynamics. The horizontal axis is nondimensionalised by the collapse time t/T_c, while the left vertical axis is nondimensionalised radial position r/R_{max} and the right vertical axis shows the equivalent bubble radius R_{eq}/R_{max}.

The openness of the conical boundary exerts a pronounced influence on both the shrink-driven flow and the evolution of wall shear stress. Under less constrained, more open boundary conditions, the boundary-induced flow promotes faster bubble shrinkage, thereby accelerating the spatial development of wall shear stress. This is evidenced by the RT curves in Fig.2, where the bubble collapse time for β = 90° is significantly shorter than that for the flat wall case (β = 180°). Comparing the wall shear stress distributions in Fig.8(a) and (b), the β = 90° case exhibits slightly higher shear stress and more rapid spatial propagation than the β = 180° case. These observations indicate that a more open conical boundary facilitates the rapid formation and outward propagation of shrink-driven flow, thereby expediting the evolution of wall shear stress. Overall, these results underscore the critical role of boundary geometry in modulating bubble dynamics and the associated wall mechanical response.

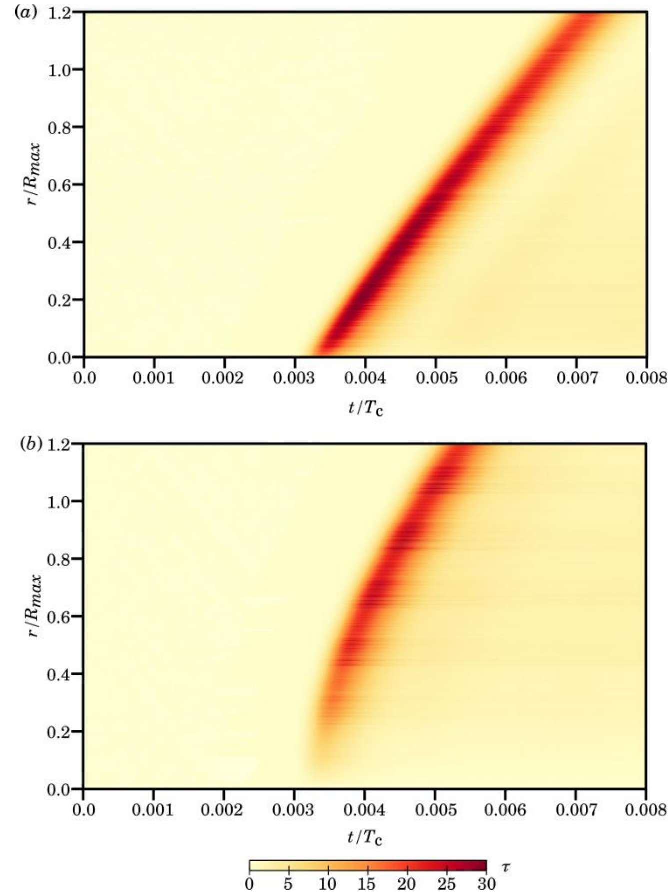

Fig.9 Zoom-in views of Fig.8 showing the spatiotemporal distribution of wall shear stress during the early expansion stage. The observed stress peaks arise from shock waves emitted during the initial bubble growth. Panel (a) corresponds to β = 90°, γ=1.0, and panel (b) toβ = 190°,γ=1.0.

During the subsequent jet formation, as shown in Fig.8(a), the emergence of the jet causes a pronounced change in the direction of the wall shear stress, accompanied by a rapid increase in its magnitude. Once the jet reaches the rigid boundary and spreads radially outward along the wall, its initial velocity of U_{jet}≈ 260 m/s gradually decays to about 160 m/s upon impact with the boundary, inducing extremely large wall shear stress with peak values around 1034 kPa. In contrast, for the β = 180° case shown in Fig.8(b), the maximum wall shear stress is only about 140 kPa, in good agreement with the results reported by Zeng (2018). Consequently, the peak wall shear stress for the β = 90° case is more than seven times higher than that for the β = 180° case, highlighting the significant influence of boundary geometry. Therefore, a more open conical boundary facilitates higher jet velocities, which in turn lead to larger wall shear stress. Additionally, regarding the fluctuations observed in the wall shear stress after the peak induced by the jet (Fig. 8(a) at t/T_c ≈1.3), similar behaviors have also been reported in previous numerical studies (Zeng, 2018; Huang, 2024). These fluctuations arise from a series of complex near-wall phenomena, including the breakup of small satellite bubbles and the backflow induced by the oscillation of the toroidal bubble.

CONCLUSIONS

This study reports numerical results on the wall shear stress generated by a cavitation bubble near a conical boundary for the reference case with γ=1.0 and $\beta = 90^o$. The computational setup was refined by improving the geometry near the cone apex and applying an appropriate boundary treatment to the conical surface, together with supplementary validation to ensure the reliability of the simulations. Based on this improved configuration, the influence of boundary geometry on bubble dynamics and jet formation was examined. Representative snapshots of the wall shear stress distribution, along with its full spatio-temporal evolution, were presented.

The results show that the cone angle β has a decisive impact on both the jet velocity and the timing of jet formation. For the more open conical boundary ($\beta = 90^o$), the jet reaches an initial velocity of approximately 260 m/s and decreases to about 160 m/s upon impact, producing a peak wall shear stress up to 1034kPa. In contrast, the corresponding peak value for the flat-wall case ($\beta = 180^o$) is only about 140 kPa, consistent with previous findings and more than seven times smaller. These results demonstrate the high sensitivity of wall shear stress to boundary geometry and indicate that a more open conical boundary promotes stronger flow convergence and thus a more intense jet.

The present study provides only a limited exploration of the parameter space. Future work will extend this investigation to systematically examine the phenomenon. In particular, the combined effects of the cone angle β, stand-off distance γ, and fluid properties such as dynamic viscosity μ will be explored to clarify their coupled influence on jet dynamics and the evolution of wall shear stress.

ACKNOWLEDGEMENTS

This work was supported by the National Key Research and Development Program of China (2025YFF0519800), to which the authors are most grateful.

REFERENCES

Cui, Pu and Zhang, A-Man and Wang, Shiping and Khoo, Boo Cheong (2018). "Ice breaking by a collapsing bubble", *Journal of Fluid Mechanics*, Vol 841, pp.287-309.

Dijkink, Rory, and Claus-Dieter Ohl (2008). "Measurement of cavitation induced wall shear stress", *Applied Physics Letters*, 93(25).

Gonzalez-Avila, S.R., Huang, X., Quinto-Su, P.A., Wu, T. and Ohl, C.-D. (2011). "Motion of micrometer sized spherical particles exposed to a transient radial flow: attraction, repulsion, and rotation", *Physical Review Letters*, 107(7), 074503.

Huang, Jianlin, Jingzhu Wang, Wenlu Guo, and Yiwei Wang(2024). "Wall vortex induced by the collapse of a near-wall cavitation bubble: Influence of the water surface." *Physical Review Fluids*, no. 5 : 053602.

Ohl, C.D., Arora, M., Dijkink, R., Janve, V. and Lohse, D. (2006). "Surface cleaning from laser-induced cavitation bubbles", *Applied Physics Letters*, 89(7).

Supponen, Outi, Obreschkow, Danail, Tinguely, Marc, Kobel, Philippe, Dorsaz, Nicolas & Farhat Mohamed (2016)"Scaling laws for jets of single cavitation bubbles.", *Journal of Fluid Mechanics*, 535-564, 169.

Tomita, Y., and A. Shima.(1986)"Mechanisms of impulsive pressure generation and damage pit formation by bubble collapse. ", *Journal of Fluid Mechanics*, 535-564, 169.

Wang, S.P., Geng, H., Zhang, S. and Wang, S.W. (2024). "Pressure waves from air gun bubbles: A numerical analysis based on the finite volume method", *Physics of Fluids*, 36(1).

Wu, Wen-Tao, Zhou, Jun-Jie, Xie, Da-Hao, and Wang, Shi-Ping (2025). "Bubble dynamics near a rigid boundary with a protruded cone", *International Journal of Multiphase Flow*, 105456, Elsevier.

Zeng, Qingyun, Hongjie An, and Claus-Dieter Ohl (2022). "Wall shear stress from jetting cavitation bubbles: Influence of the stand-off distance and liquid viscosity", *Journal of Fluid Mechanics*, 932, A14.

Zeng, Qingyun, Silvestre Roberto Gonzalez-Avila, Rory Dijkink, Phoevos Koukouvinis, Manolis Gavaises, and Claus-Dieter Ohl (2018). "Wall shear stress from jetting cavitation bubbles", *Journal of Fluid Mechanics*, 846, 341–355.

Zhang, A-Man, Shi-Min Li, Run-Ze Xu, Shao-Cong Pei, Shuai Li, and Yun-Long Liu (2024). "A theoretical model for compressible bubble dynamics considering phase transition and migration", *Journal of Fluid Mechanics*, 999, A58.